Supplementary information

Abnormally low thermal conductivity of Co_2MnO_4 spinel induced by cation inversion

Qi Ye,[II][a][b] Shengyang Wang,[II][b] Huilan Ma[a][b], Wen Yin[c], Zhongbo Hu[a], and Can Li*[a][b]

[a.] *University of Chinese Academy of Sciences, Beijing 100049, P. R. China.*

[b.] *State Key Laboratory of Catalysis, Dalian Institute of Chemical Physics, Chinese Academy of Sciences, Dalian 116023, P. R. China.*

[c.] *Spallation Neutron Source Science Center, Dongguan 523803, P. R. China.*

II: equally contribution to the manuscript

Experimental methods

Preparation of spinel materials

The preparation procedures of Co_2MnO_4 spinel samples were taken as examples, and $CoMn_2O_4$ samples were prepared with similar methods.

Hydrothermal synthesis: $Co(Ac)_2 \cdot 4H_2O$ (0.06 mol, 99.9%, MACKLIN) and $Mn(Ac)_2 \cdot 4H_2O$ (0.03 mol, 99.9%, MACKLIN) were dissolved in DI water (100 mL), respectively. Then, $NH_3 \cdot H_2O$ was added dropwise into the Co solution until the $Co(OH)_2$ sediment was completely dissolved to form dissolved $Co(NH_3)_6^{2+}$ ions. The solution was stirred in air atmosphere until the greenish Co(II) solution was oxidized into a brownish Co(III) solution. Afterward, the Mn solution was added to the Co solution, and the mixture was stirred for 5 min (For preparation of $CoMn_2O_4$, the Co solution was added to the Mn solution in a molar ratio of 1:2). The solution was then transferred into a Teflon-lined stainless-steel autoclave and maintained at 150 °C for 10 h. After a sufficient hydrothermal reaction, the solid sample was collected by

centrifugation and dried in air.

The $NiCo_2O_4$, $NiFe_2O_4$, and $ZnCo_2O_4$ samples were prepared by the same hydrothermal method with 10 h reactions at 190, 180, and 190 °C, respectively.

Sol-gel synthesis: The aqueous solutions of $Co(Ac)_2 \cdot 4H_2O$ and $Mn(Ac)_2 \cdot 4H_2O$ were prepared as described above, followed by addition of citric acid (90 mmol) and EDTA (60 mmol in the final dispersion) with stirring, and the mixture was stirred for 1 h. Then, $NH_3 \cdot H_2O$ was added dropwise to adjust the pH to 6–8, followed by the addition of the same amount of ethanol as that of DI water. The colloidal sol was preserved at 120 °C to form a gel. Finally, the solid mixture was calcinated at 600 °C to form the spinel samples.

Nitrate decomposition synthesis: $Co(NO_3)_2 \cdot 6H_2O$ (0.06 mol, 99.9%, MACKLIN) and $Mn(NO_3)_2 \cdot 4H_2O$ (0.03 mol, 99.9%, MACKLIN) were dissolved in DI water (100 mL), respectively. Then, the Mn solution was added into the Co solution with strong stirring (For preparation of $CoMn_2O_4$, the Co solution was added to the Mn solution in a molar ratio of 1:2), followed by stirring and vaporization at 80 °C. Afterwards, the slurry obtained was calcinated at 250 °C for 2 h for the decomposition of nitrates. The resulting solid was then grounded, pressed into pellets, and calcinated at high temperature (500–900 °C) for 8 h to obtain spinel-type oxide samples.

Solid-state synthesis: Co_3O_4 and MnO solid powders were mixed in a stoichiometric ratio and then dispersed in ethanol, followed by a ball-milling for 20 h. After centrifuged and dried, the mixed powder was collected and pelleted. The pellets were calcinated at 1000 °C for 20 h to obtain the spinel samples.

Material characterizations

The powder X-ray diffraction patterns (XRD) were recorded using an X-ray diffractometer (Smartlab, Rigaku) with Cu K_α radiation (1.5406 Å) at room temperature under air atmosphere. The time-of-flight (TOF) powder neutron diffraction experiments were conducted on a multi-physics instrument (MPI) from China Spallation Neutron Source (CSNS). Rietveld refinements were performed on Fullprof software with the XRD and TOF ND data. The sample morphology was

revealed by a field emission scanning electron microscope (SEM, Quanta-200, FEI). The sample microstructure was probed by a transmission electron microscope (TEM, TECNAI G2 F30, FEI) together with the selected area electron diffraction (SAED). The Raman spectra were collected on a confocal Raman spectrometer (Invia, Renishaw plc.) using a 785 nm laser source under air atmosphere. All the spectra were collected under the laser power of 0.6 mW. The element ratio of the samples was measured using an inductively coupled plasma (ICP) optical emission spectrometer (ICPS-8100, SHIMADZU).

The electrical property of the samples was measured using a Hall effect analyzer (Accent HL5500 Hall System). The thermal stability of the sample was evaluated by using a thermalgravimetric analyzer (Diamond TG/DTA, PE) for thermogravimetry (TG) and differential thermal analysis (DTA) with a gradual heating in air atmosphere. An empty alumina crucible was used as the inert reference material in the DTA measurement. The thermal diffusion coefficients at different temperatures were measured by the laser flash method (LFA 467HT, Netzsch) in an argon atmosphere. The thermal conductivity was calculated by $\kappa = \alpha \times \rho \times C_p$, where α is the thermal diffusion coefficient measured by LFA, ρ is the apparent density obtained by dividing the sample mass by its volume (calculated by the measured thickness and radius of the cylindric sample), and C_p is the heat capacity estimated by the Dulong-Petit principle as $C_p = C_V = 3nR/M$, where R is the universal gas constant, n is the number of atoms in the unit cell, and M is the molecular mass of the unit cell. The cylindric pellets were prepared by uniaxial pressing at about 280 MPa with diameters of $\varphi = 12.7$ mm followed by sintering.
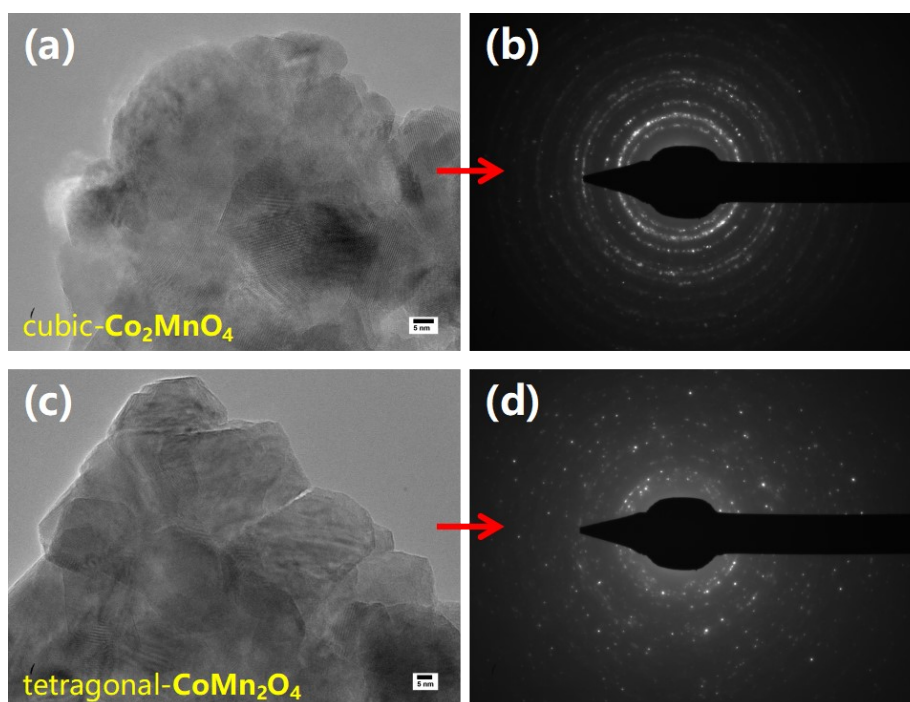
Micro structures characterizations

Figure S1. **(a,c)** TEM images and **(b,d)** SAED patterns (collected in the area of (a) and (c), respectively) of Co_2MnO_4 and $CoMn_2O_4$ spinel samples. The diffraction rings in SAED patterns indicate the polycrystal structure of the samples.

Scanning electron microscopy (SEM) images reveal that the sol-gel prepared samples have the morphology of nanocrystal accumulation, and the average grain size is around 0.15 μm (Figure S2). For samples prepared by solid-state method, the grain sizes are much larger, ranging from 0.5 to 5 μm, due to the higher calcination temperature.
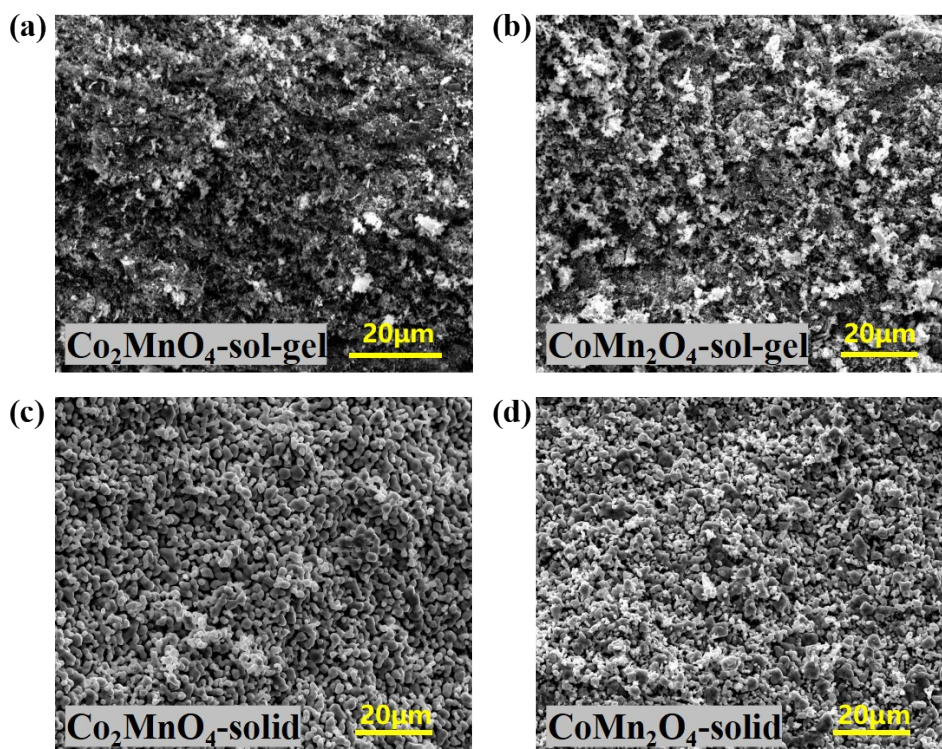
Figure S2. SEM images for the fractured surfaces of the pressed pellets of spinel samples synthesized by sol-gel method and solid-state method with annealing temperature at 600 and 1000 °C, respectively. **(a)** Co_2MnO_4, sol-gel, 600 °C, **(b)** $CoMn_2O_4$, sol-gel, 600 °C, **(c)** Co_2MnO_4, solid-state, 1000 °C, and **(d)** $CoMn_2O_4$, solid-state, 1000 °C.

First principle theoretical calculations

The first principle DFT calculations were conducted with the Vienna Ab initio Simulation Package (VASP)[1, 2]. The projector augmented wave (PAW)[3] pseudopotentials were used to describe the valence electron-core ion interactions. The electron exchange correlation interactions were approximated by generalized-gradient approximation (GGA) with the Perdew–Burke–Ernzerhof (PBE)[4] functional. A rotational invariant type GGA+U method[5] was employed to describe the TM-3d electronic structures more precisely, and the U values were chosen to be 3.9 and 3.32 eV for Mn and Co, respectively. Spin-polarization is considered in all the calculations. The first Brillouin zone was sampled by a $6 \times 6 \times 6$ k-point mesh with the

Monkhorst–Pack scheme, and the cut-off energy for plane waves was set to be 520 eV. The lattice parameters and atomic positions of a prime cell containing 14 atoms were fully relaxed during geometry optimizations to reach a convergence with forces on atoms less than 1E-8 eV Å^{-1} and electronic energies less than 1E-8 eV. The harmonic phonon properties including phonon dispersion were derived from the second-order interatomic force constants calculated by density functional perturbation theory (DFPT). In DFPT calculations, $2 \times 2 \times 2$ supercells containing 112 atoms and a k-point mesh of $3 \times 3 \times 3$ were used.

The lattice thermal conductivities (LTCs) were calculated by solving the BTE[6] with relaxation-time approximation (RTA) based on the calculated third-order interatomic force constants. The linearized phonon Boltzmann equation for LTC calculations is

$$v_\lambda \cdot \nabla T \frac{\partial n_\lambda^o}{\partial T} = \left(\frac{\partial n_\lambda}{\partial t} \right)_{\text{collision}} ,$$

in which the v_λ is the phonon group velocity of the mode $\lambda(\omega, q)$, n_λ^o and $n_\lambda = n_\lambda^0 + n_\lambda^1$ are the equilibrium and non-equilibrium phonon distribution function.[7, 8] The right hand side is the collision term describing the phonon-phonon scattering, which is the integration of all the possible scattering mechanisms into and out of the state λ.[9, 10] In the commonly used relaxation time approximation (RTA), the collision integration is reduced to $-n_\lambda^1 / \tau_\lambda^{SMRT}$, from which the single mode relaxation time (SMRT) τ_λ^{SMRT} is derived.[8, 11] The phonon lifetime in thermal conductivity calculation is employed as $\tau_\lambda = \tau_\lambda^{SMRT}$, and the mode specific phonon mean free path is then derived from the phonon lifetime and group velocity by $\Lambda_\lambda = v_\lambda \cdot \tau_\lambda$.[12] The above calculations were conducted using the Phonopy[13] and Phono3py[14] codes.

The LTCs of Co-Mn spinels

The calculated results of the cubic Co$_2$MnO$_4$ and tetragonal CoMn$_2$O$_4$ are shown

in Figure S3. The calculated volumetric heat capacity shows no significant difference between the two phases, and the capacity of the tetragonal phase is even slightly higher than that of the cubic phase. The phonon group velocity of the cubic phase is slightly higher than that of the tetragonal phase in the low-frequency region, indicating a better heat transport ability of acoustic phonons in Co_2MnO_4. Since the effects of capacity and phonon group velocity are not decisive factors, the difference in LTC should mainly originate from the difference in phonon MFP. The phonon MFP plays a decisive role in heat transport, where higher MFP signifies less phonon scattering and thus higher LTC.
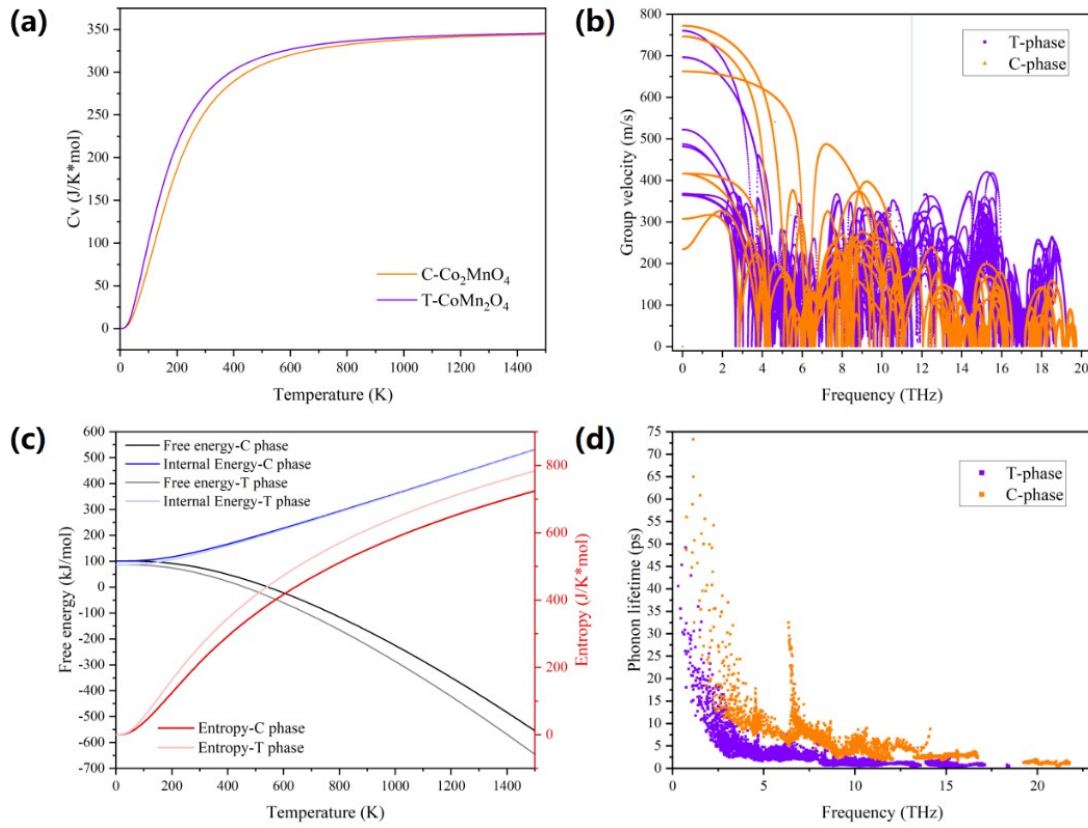
Figure S3. First principle theoretical calculations on the phonon properties of the cubic Co_2MnO_4 and tetragonal $CoMn_2O_4$ spinels. **(a)** Phonon heat capacity and **(c)** free energy and entropy as a function of temperature; **(b)** phonon group velocity and **(d)** phonon lifetime as a function of phonon frequency.
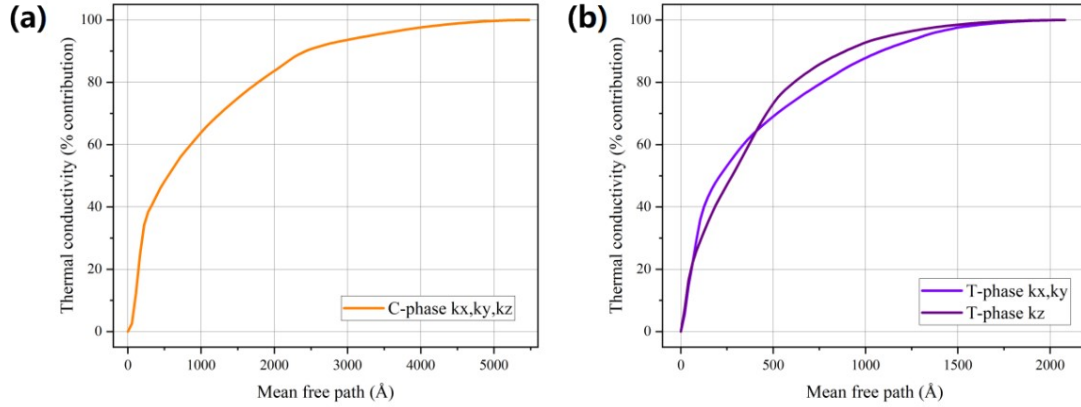
Figure S4. Accumulated lattice thermal conductivities calculated as a function of phonon mean free path (MFP) of **(a)** cubic Co_2MnO_4 and **(b)** tetragonal $CoMn_2O_4$ spinels.

Grüneisen parameter

The Grüneisen parameter γ is a quantitative description of the lattice anharmonicity and has an inverse relationship with LTC. Higher γ often indicates stronger anharmonic phonon-phonon interaction, which reduce the phonon lifetime and thermal conductivity.[15, 16]

The mode Grüneisen parameter isdefined as

$$\gamma_\lambda = -\frac{V}{\omega_\lambda} \cdot \frac{\partial \omega_\lambda}{\partial V}$$

where V is the cell volume, $\lambda(\omega, q)$ is the specific phonon mode. With the perturbation treatment, the Grüneisen parameter can be derived as a function of the quadratic and anharmonic 3rd interatomic force constants (IFCs) as

$$\gamma_\lambda = \frac{1}{6\omega_\lambda^2} \sum_{ijk,bc,\alpha\beta} \Psi_{ijk}^{\alpha\beta\gamma}(0,b,c) \frac{X_{is}^{*\alpha}(q)X_{js}^{\beta}(q)}{\sqrt{M_i M_j}} \tau_k^{\delta} e^{iq \cdot R_b}$$

where Ψ is the 3rd IFC, X is the eigen modes derived from the 2nd dynamic matrix, M is the atomic mass, τ indicates the atom position and R is the lattice vector.[15, 17]

Slack's equation[18] is commonly used for estimating the magnitude of LTC of nonmetallic crystals:

$$\kappa_{\mathrm{L}} = B \frac{\overline{M} \delta \theta^3}{N^{2/3} T \gamma^2}$$

where B is a constant, N is the number of atoms in the unit cell, M is the average atomic mass in the crystal, δ^3 is the average volume occupied by one atom, θ is the Debye temperature, and γ is the Grüneisen parameter. The calculated Grüneisen parameters of $CoMn_2O_4$ spinel have higher absolute values than those of the Co_2MnO_4 spinel.
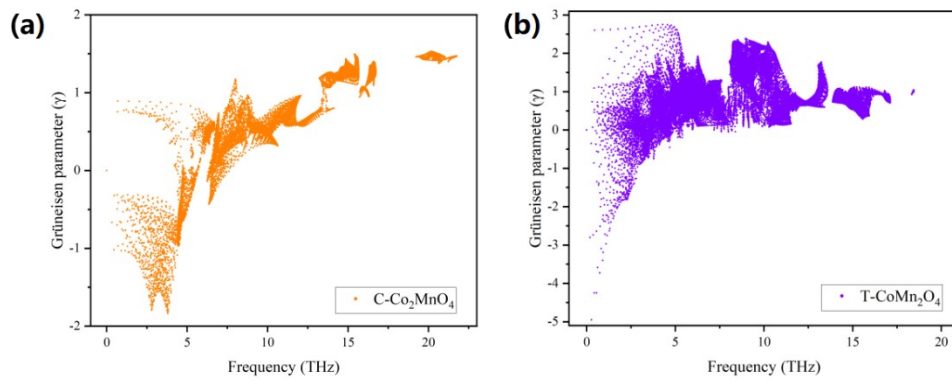

Figure S5. Calculated Grüneisen parameters of **(a)** cubic Co_2MnO_4 and **(b)** tetragonal $CoMn_2O_4$ spinels.

Cation inversion calculations
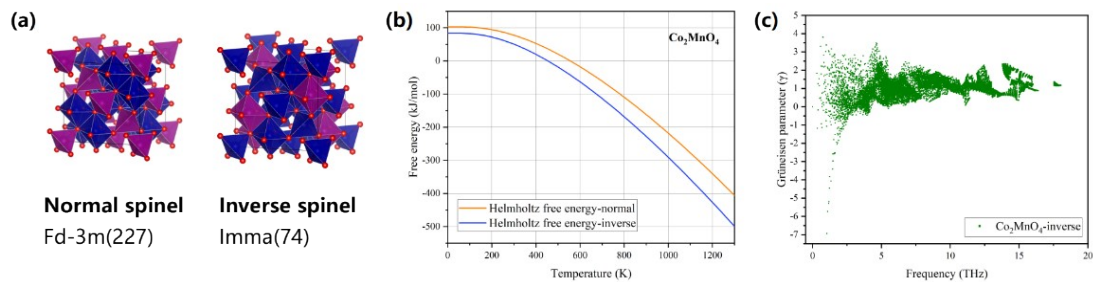
Figure S6. (a) Crystal structures of the normal and inverse Co_2MnO_4 spinels; **(b)** Calculated Helmholtz free energies of normal and inverse Co_2MnO_4 spinels as a function of temperature; **(c)** Grüneisen parameters of the inverse Co_2MnO_4 spinel.

Among all four possible partially inversed structures, the structure *inverse-1* exhibits the lowest total energy comparing to the other three structures. The calculated phonon dispersion also indicates that the structures with higher energy are dynamically unstable. Therefore, we determined the structure *inverse-1* as the only possible partially inversed spinel phase in our calculations.

Figure S7. Structure of the normal cubic Co_2MnO_4 spinel and 4 possible partially inversed phases with the corresponding phonon dispersion.
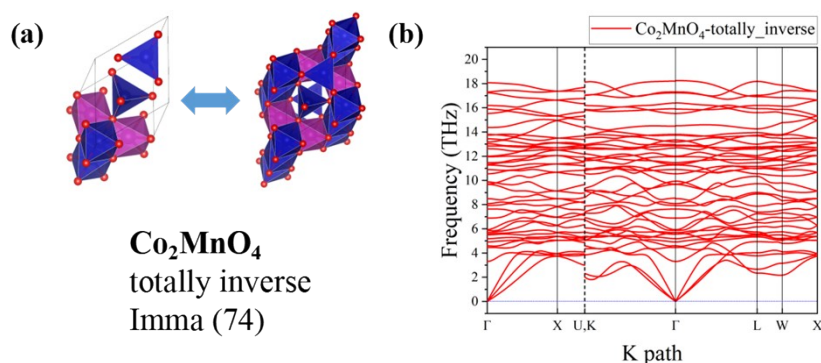
Figure S8. (a) Crystal structure and **(b)** calculated phonon dispersion of the totally inversed Co_2MnO_4 spinel in the form of a prime cell with a space group of *Imma*.

Electronic thermal conductivities

The electrical resistivities, carrier concentrations, and Hall mobilities of Co_2MnO_4 and $CoMn_2O_4$ samples are shown in Table S1. The electronic thermal conductivities (κ_e) are estimated by Wiedemann-Franz law: $\kappa_e = L\sigma T$, where σ is the electrical conductivity, T is the absolute temperature, and L is the Lorenz number estimated by the Sommerfeld value of $L_0 = (\pi^2/3) * (k_B/e)^2 = 2.44 \times 10^{-8}$ W*Ω*K^{-2} (where k_B is the Boltzmann constant and e is the electron charge). The electronic thermal conductivities of both the cubic and tetragonal spinel samples show negligible values compared with the measured total thermal conductivities.

Table S1. Electrical resistivities, carrier concentrations, Hall mobilities, and electronic thermal conductivities estimated by the Wiedemann-Franz law for Co_2MnO_4 and $CoMn_2O_4$ samples at room temperature.

Samples	Electrical resistivity [Ω cm]	Carrier concentration [cm^{-3}]	Carrier mobility [$cm^2 V^{-1} s^{-1}$]	κ_e (300 K) [$W m^{-1} K^{-1}$]
Co_2MnO_4-1000	8.108×10^2	1.39×10^{16}	0.554	9.03×10^{-7}
$CoMn_2O_4$-1000	2.617×10^6	1.10×10^{13}	0.217	2.80×10^{-10}

XRD patterns and Rietveld refinement parameters
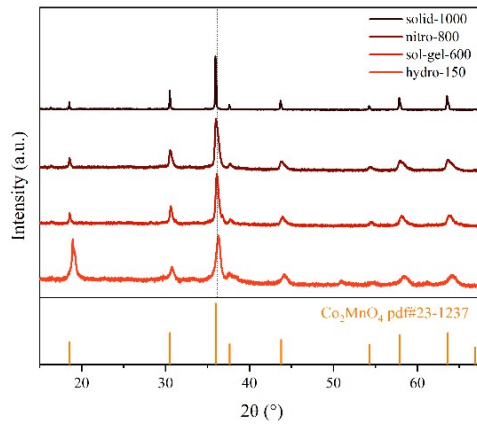
Figure S9. XRD patterns of the Co_2MnO_4 samples synthesized by four methods, as well as the PDF standard card #23-1237 for Co_2MnO_4.
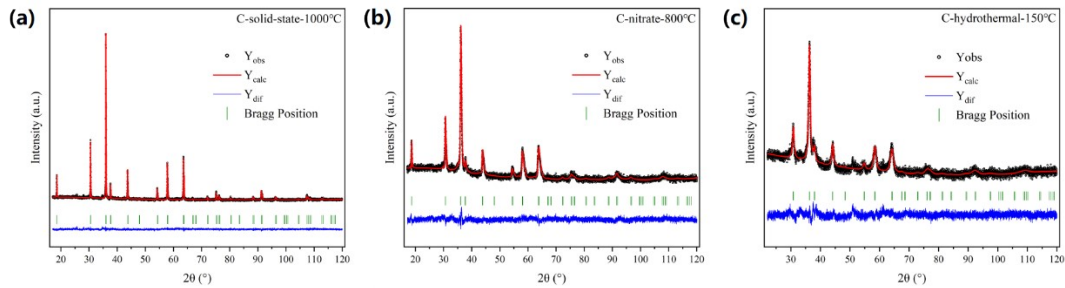

Figure S10. XRD patterns and Rietveld refinements of Co_2MnO_4 samples synthesized by **(a)** solid-state method (1000 °C), **(b)** nitrate decomposition method (800 °C), and

(c) hydrothermal method (150 °C).

Table S2. Rietveld refinement parameters on the **XRD** patterns of cubic Co_2MnO_4 spinel samples synthesized by four methods and the tetragonal $CoMn_2O_4$ sample synthesized by sol-gel method at 600 °C.

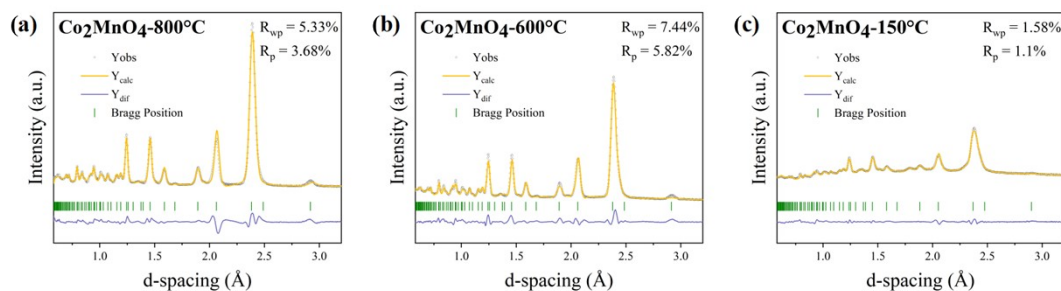| Samples	Chi^2	R_{wp}	R_p	Lattice parameters [Å]	Cation inversion degree δ [%]	O atom position (x*x*x)
Co_2MnO_4-150	1.21	1.49	1.17	8.207	33.29	0.26164
Co_2MnO_4-600	1.12	1.42	1.16	8.235	61.27	0.25797
Co_2MnO_4-800	1.22	1.47	1.17	8.257	85.46	0.25736
Co_2MnO_4-1000	1.13	1.43	1.12	8.273	90.84	0.25555
$CoMn_2O_4$-1000	1.56	2.25	1.75	a = b = 5.723 c = 9.283	0.00	\

Figure S11. TOF neutron diffraction patterns and Rietveld refinements of Co_2MnO_4 samples synthesized by **(a)** nitrate decomposition method (800 °C), **(b)** sol-gel method (600 °C), and **(c)** hydrothermal method (150 °C).

Table S3. Rietveld refinement parameters on the **TOF neutron diffraction** patterns of the cubic Co_2MnO_4 spinel samples synthesized by four methods and the tetragonal $CoMn_2O_4$ sample synthesized by solid-state method at 1000 °C.

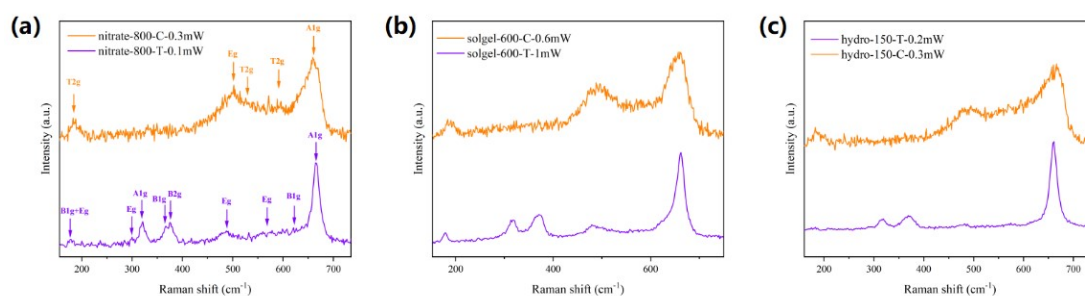| Samples	Chi^2	R_{wp}	R_p	Lattice parameters [Å]	Cation inversion degree δ [%]	O atom position (x*x*x)
Co$_2$MnO$_4$-150	18.6	1.58	1.1	8.207	38.64	0.26549
Co$_2$MnO$_4$-600	4.52	7.44	5.82	8.241	69.60	0.26356
Co$_2$MnO$_4$-800	4.52	7.44	5.82	8.253	88.61	0.26258
Co$_2$MnO$_4$-1000	18.6	1.58	1.1	8.264	94.20	0.26223
CoMn$_2$O$_4$-1000	203	8.03	5.92	a = b = 5.721 c = 9.271	0.00	\

Raman spectra

Figure S12. Raman spectra of Co$_2$MnO$_4$ samples synthesized by **(a)** nitrate decomposition method (800 °C), **(b)** sol-gel method (600 °C), and **(c)** hydrothermal method (150 °C). The measurements were conducted at room temperature under air atmosphere with a laser source of 785 nm wavelength.
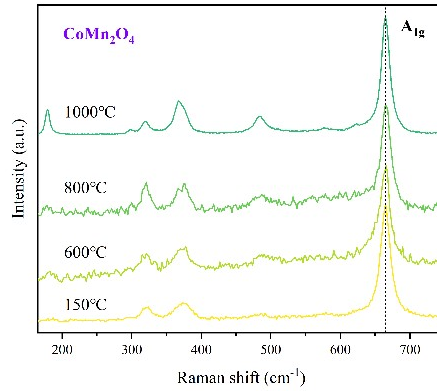
Figure S13. Raman spectra of $CoMn_2O_4$ samples synthesized by four methods. The measurements were conducted at room temperature under air atmosphere with a laser source of 785 nm wavelength. The unchanged position of the A_{1g} peak indicates that the occupation of cations does not vary with different synthesis methods and varied annealing temperatures.
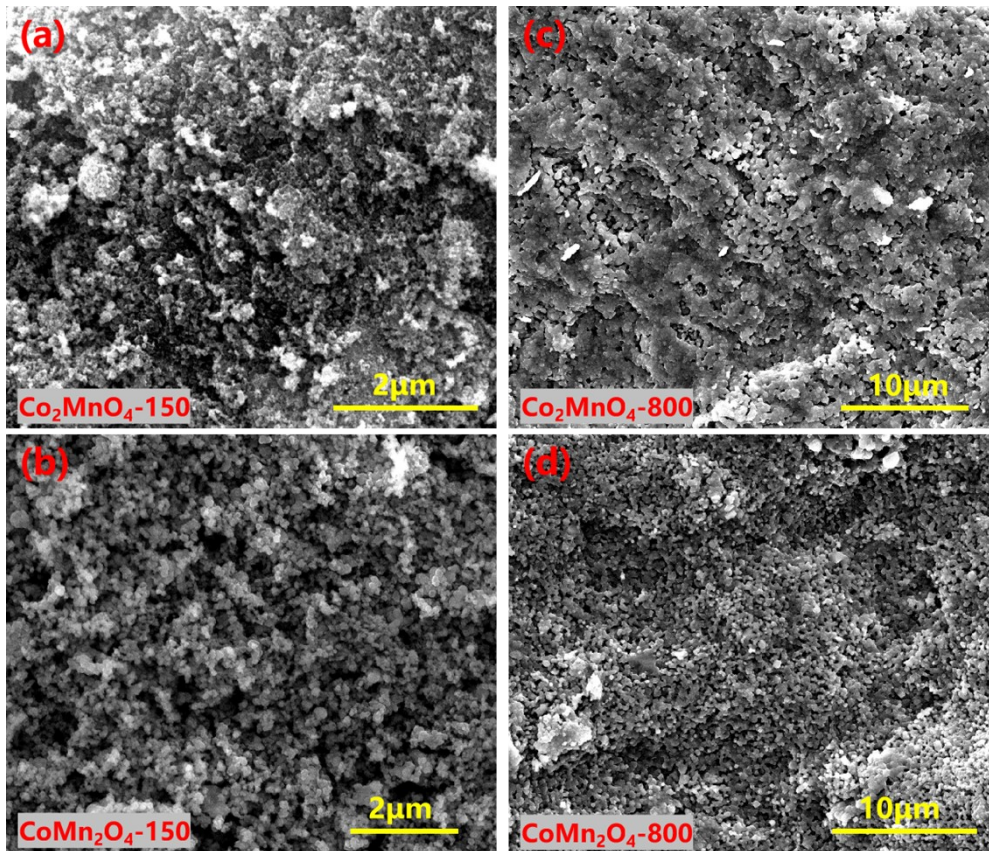

Figure S14. SEM images for the fractured surfaces of the pressed pellets of spinel samples with different annealing temperatures. **(a)** Co_2MnO_4, 150 °C; **(b)** $CoMn_2O_4$,

150 °C; **(c)** Co$_2$MnO$_4$, 800 °C; **(d)** CoMn$_2$O$_4$, 800 °C. The grain sizes increase with the increase of annealing temperature. At the same annealing temperature, the grain sizes of the Co$_2$MnO$_4$ and CoMn$_2$O$_4$ samples are almost identical with each other.
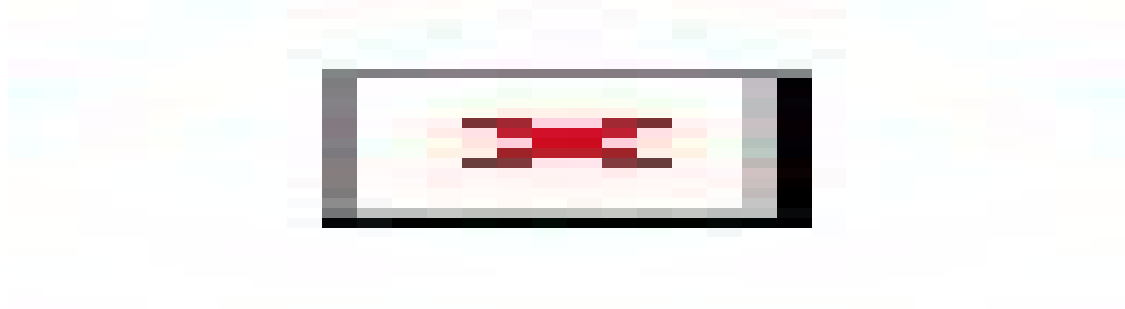

Figure S15. (a) In-situ XRD patterns of the Co$_2$MnO$_4$-150 sample with temperature rising. XRD patterns and Rietveld refinements of **(b)** the sample at 800 °C and **(c)** the sample cooled down to RT.

Table S4. Rietveld refinement parameters on the in-situ XRD patterns of the Co$_2$MnO$_4$-150 sample, comparing to the sample Co$_2$MnO$_4$-800.

Samples	R_{wp}	R_p	Chi^2	Lattice parameters [Å]	Cation inversion degree δ [%]	O atom position (x*x*x)
Co$_2$MnO$_4$-150, RT	1.49	1.17	1.21	**8.207**	33.29	0.26164
Co$_2$MnO$_4$-150, insitu 800°C	1.39	1.11	0.918	**8.341**	83.52	0.25959
Co$_2$MnO$_4$-150, 800°C cool to RT	1.40	1.12	0.876	**8.260**	83.62	0.26063
Co$_2$MnO$_4$-800, RT	1.47	1.17	1.22	**8.257**	85.46	0.25736

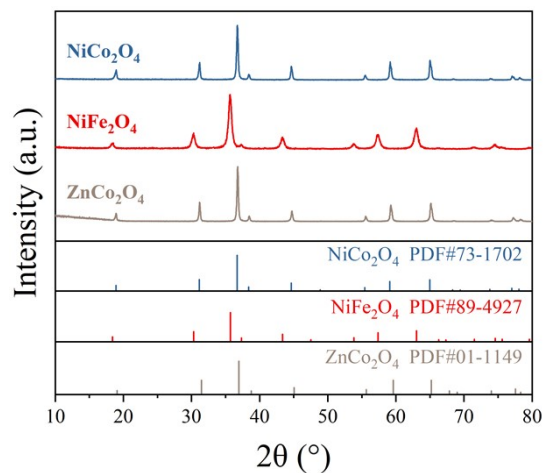**NiCo$_2$O$_4$, NiFe$_2$O$_4$, and ZnCo$_2$O$_4$ spinels**

Figure S16. XRD patterns of $NiCo_2O_4$, $NiFe_2O_4$, and $ZnCo_2O_4$ spinel samples synthesized by hydrothermal method and the corresponding PDF standard cards.
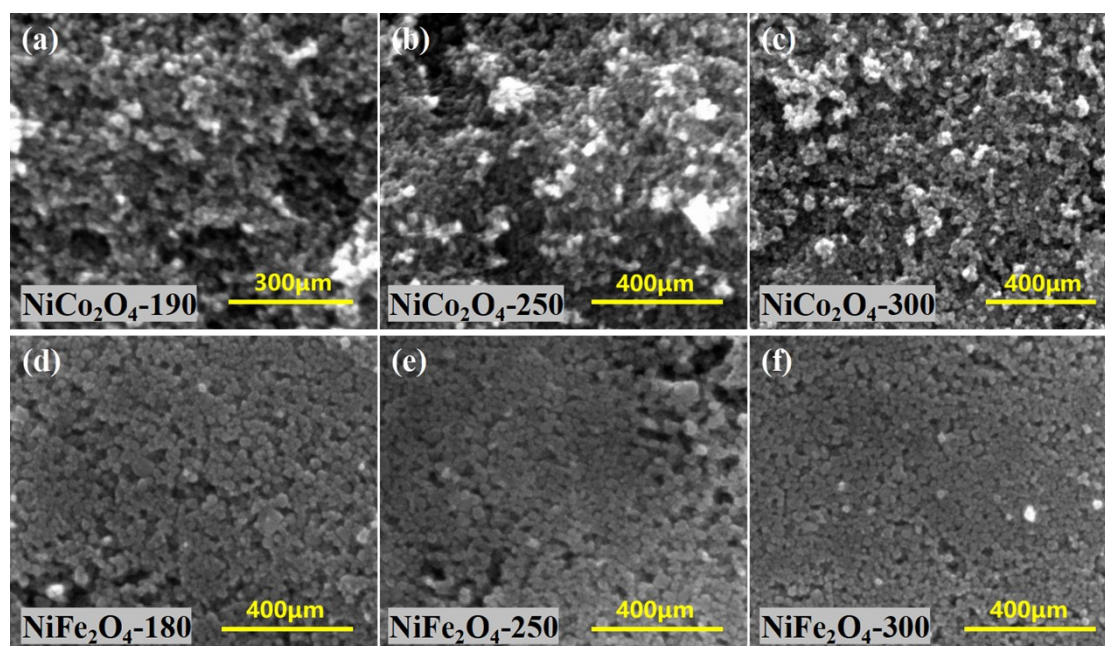

Figure S17. SEM images for the fractured surfaces of the pressed pellets of $NiCo_2O_4$ spinel samples prepared at different annealing temperatures of **(a)** 190 °C, **(b)** 250 °C, **(c)** 300 °C; and $NiFe_2O_4$ spinels prepared at annealing temperatures of **(d)** 180 °C, **(e)** 250 °C, and **(f)** 300 °C. The changes in grain size and morphology of the spinel samples annealed at 180–300 °C are unnoticeable.
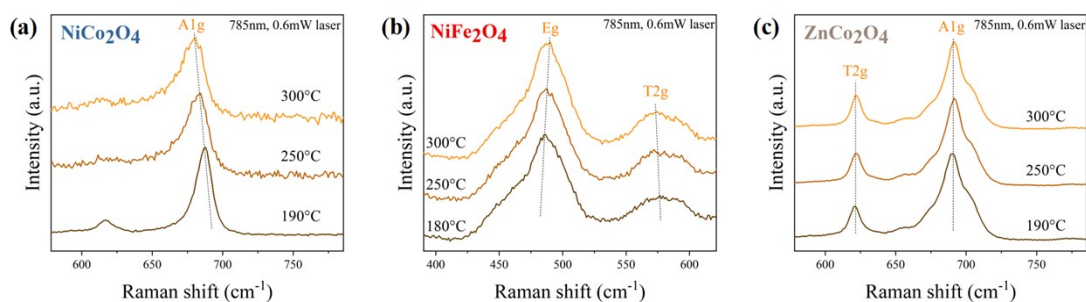
Figure S18. Raman spectra of **(a)** $NiCo_2O_4$, **(b)** $NiFe_2O_4$, and **(c)** $ZnCo_2O_4$ spinel samples at different annealing temperatures.
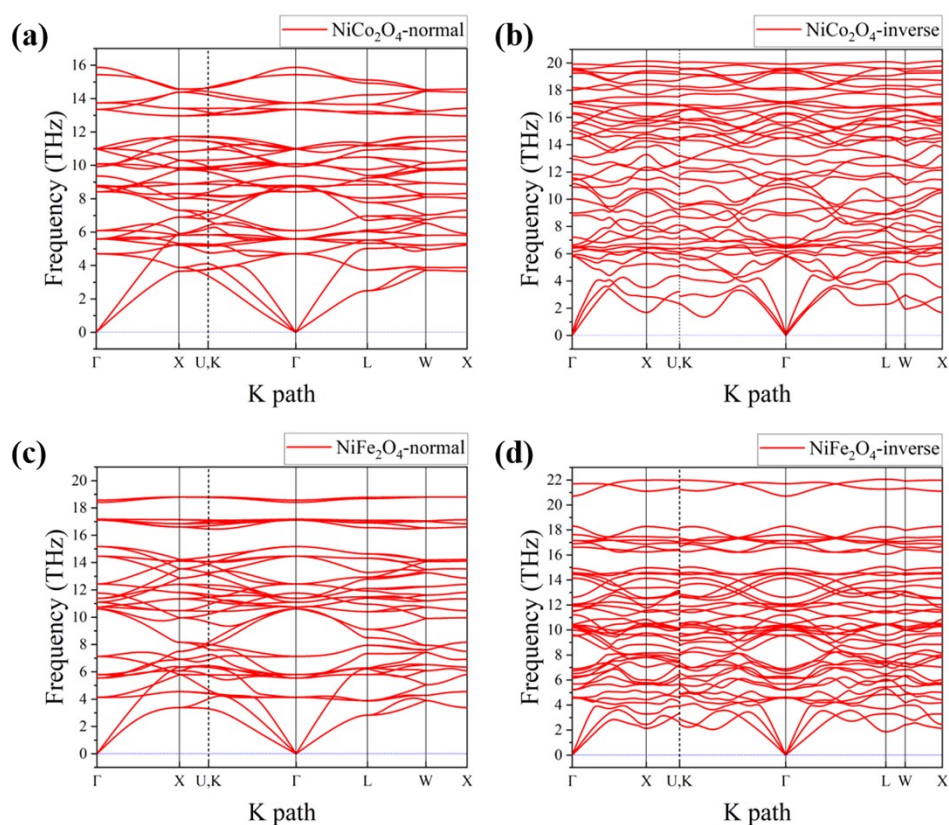

Figure S19. Calculated phonon dispersions of **(a)** normal and **(b)** inverse $NiCo_2O_4$ spinel, and **(c)** normal and **(d)** inverse $NiFe_2O_4$ spinel.

Table S5. Co-Mn element ratios and corresponding chemical formulas derived from ICP-OES.

Samples (Co/Mn ratio)	Co/Mn ratio by ICP	Chemical formula by ICP

0.5	0.5055	$Co_{1.993}Mn_{1.007}O_4$
1.5	1.5253	$Co_{1.188}Mn_{1.812}O_4$
2.0	2.0439	$Co_{0.986}Mn_{2.014}O_4$

Structure characterization on $Co_xMn_{3-x}O_4$

The $Co_xMn_{3-x}O_4$ samples were prepared by sol-gel method with annealing temperature at 600 °C, and the Co/Mn ratio was tuned by changing the ratio of ingredients. The Co/Mn atomic ratios of three typical samples were measured by inductively coupled plasma (ICP) optical emission spectrometry, and the measured Co/Mn ratio is close to the corresponding ingredient proportion employed for preparation of the specific sample (Table S5). The structural evolution of the samples with changing Co/Mn ratios was characterized by XRD patterns and Raman spectra.
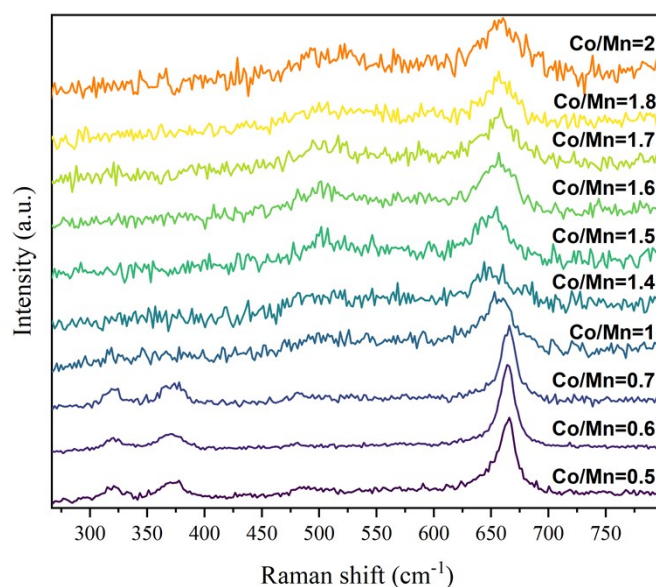

Figure S20. Raman spectra of $Co_xMn_{3-x}O_4$ samples.

Thermal conductivity calibration

For a better consistency between the experiment and theoretical calculations, we

18

adopt the relative density calibration for all the measured thermal conductivity values to exclude the influence of pores. The comprehensive effect of the porosity on the thermal conductivity can be described by Effective Medium Theory (EMT) equation[19]:

$$v \cdot \frac{\kappa_s - \kappa}{\kappa_s + 2\kappa} + (1-v) \cdot \frac{\kappa_{air} - \kappa}{\kappa_{air} + 2\kappa} = 0$$

in which κ, κ_{air} and κ_s are the thermal conductivity of the porous sample, air and solid material, v is the volume fraction of the solid, which equals to the the value of relative density. Therefore, taking the measured thermal conductivity as κ, the thermal conductivity of the solid κ_s can be derived as

$$\kappa_s = \kappa \cdot \frac{(3v-2) \cdot \kappa_{air} + 2\kappa}{2\kappa_{air} + (3v-1) \cdot \kappa}$$

The theoretical density of t-CoMn$_2$O$_4$, normal c-Co$_2$MnO$_4$, and totally inversed Co$_2$MnO$_4$ spinels are 4.86, 5.57, and 5.24 g/cm^3 respectively. For all the Co$_2$MnO$_4$ spinel samples, the theoretical density value of 5.37 g/cm^3 is used, which stands for a partially inversed spinel. The thermal conductivity of air used here is 0.026 W/m*K. The revised thermal conductivity and parameters of all the measured samples are displayed below in Table S6, including the mass, relative density and thickness.

Table S6. Theoretical and relative density, measured thermal conductivity and calibrated thermal conductivity of the spinel samples.

Samples	Theoretical density [g/cm^3]	Relative density [%]	Thickness [mm]	Mass [g]	$\kappa_{measured, 25\,°C}$ [W/m*K]	$\kappa_{calibrated, 25\,°C}$ [W/m*K]
Co$_2$MnO$_4$-150	5.37	43.59	1.113	0.330	0.254	1.193
Co$_2$MnO$_4$-600	5.37	50.05	1.166	0.397	0.235	0.745
Co$_2$MnO$_4$-800	5.37	61.10	0.818	0.340	0.646	1.474
Co$_2$MnO$_4$-1000	5.37	64.74	0.815	0.359	1.020	2.107

CoMn$_2$O$_4$-150	4.86	49.44	1.117	0.340	0.327	1.139
CoMn$_2$O$_4$-600	4.86	51.92	1.242	0.397	0.588	1.934
CoMn$_2$O$_4$-800	4.86	60.29	0.943	0.350	1.760	4.269
CoMn$_2$O$_4$-1000	4.86	62.94	0.873	0.338	2.874	6.402
Co/Mn: 0.6	4.92	51.81	1.225	0.396	0.435	1.398
Co/Mn: 0.7	4.98	51.76	1.216	0.397	0.354	1.113
Co/Mn: 1.0	5.11	52.92	1.231	0.422	0.357	1.065
Co/Mn: 1.4	5.24	52.54	1.420	0.496	0.270	0.786
Co/Mn: 1.5	5.27	47.20	1.565	0.493	0.117	0.342
Co/Mn: 1.6	5.29	48.95	1.493	0.490	0.138	0.397
Co/Mn: 1.7	5.31	52.74	1.390	0.494	0.176	0.469
Co/Mn: 1.8	5.34	47.30	1.220	0.390	0.198	0.691
ZnCo$_2$O$_4$-190	6.07	60.11	0.531	0.242	0.599	1.409
ZnCo$_2$O$_4$-250	6.07	62.11	0.552	0.259	1.034	2.324
ZnCo$_2$O$_4$-300	6.07	62.27	0.675	0.318	1.222	2.744
NiCo$_2$O$_4$-190	5.49	46.84	1.092	0.350	0.328	1.323
NiCo$_2$O$_4$-250	5.49	46.94	0.965	0.310	0.297	1.168
NiCo$_2$O$_4$-300	5.49	46.99	1.188	0.382	0.284	1.102
NiFe$_2$O$_4$-180	5.49	51.56	0.964	0.340	0.604	2.029
NiFe$_2$O$_4$-250	5.49	49.25	1.007	0.340	0.503	1.874
NiFe$_2$O$_4$-300	5.49	46.12	1.073	0.339	0.408	1.789

References

1. G. Kresse and J. Furthmüller, *Physical Review B*, 1996, **54**, 11169-11186.
2. G. Kresse and J. Furthmüller, *Computational Materials Science*, 1996, **6**, 15-50.
3. P. E. Blöchl, *Physical review B*, 1994, **50**, 17953.
4. J. P. Perdew, K. Burke and M. Ernzerhof, *Physical review letters*, 1996, **77**, 3865.
5. S. L. Dudarev, G. A. Botton, S. Y. Savrasov, C. Humphreys and A. P. Sutton, *Physical Review B*, 1998, **57**, 1505.
6. J. M. Ziman, *Principles of the Theory of Solids*, Cambridge university press, 1972.
7. A. Ward, D. A. Broido, D. A. Stewart and G. Deinzer, *Physical Review B*, 2009, **80**, 125203.

8.	D. A. Broido, M. Malorny, G. Birner, N. Mingo and D. A. Stewart, *Applied Physics Letters*, 2007, **91**.

9.	M. Asen-Palmer, K. Bartkowski, E. Gmelin, M. Cardona, A. Zhernov, A. Inyushkin, A. Taldenkov, V. Ozhogin, K. M. Itoh and E. Haller, *Physical review B*, 1997, **56**, 9431.

10.	D. Broido, A. Ward and N. Mingo, *Physical Review B—Condensed Matter and Materials Physics*, 2005, **72**, 014308.

11.	P. B. Allen and V. Perebeinos, *Physical Review B*, 2018, **98**, 085427.

12.	A. Togo, *Journal of the Physical Society of Japan*, 2022, **92**, 012001.

13.	A. Togo and I. Tanaka, *Scripta Materialia*, 2015, **108**, 1-5.

14.	A. Togo, L. Chaput and I. Tanaka, *Physical Review B*, 2015, **91**, 094306.

15.	C. H. Lee and C. K. Gan, *Physical Review B*, 2017, **96**, 035105.

16.	X. Qian, J. Zhou and G. Chen, *Nat Mater*, 2021, DOI: 10.1038/s41563-021-00918-3.

17.	F. Bottin, J. Bieder and J. Bouchet, *Computer Physics Communications*, 2020, **254**, 107301.

18.	G. A. Slack, *Journal of Physics and Chemistry of Solids*, 1973, **34**, 321-335.

19.	J. Wang, J. K. Carson, M. F. North and D. J. Cleland, *International Journal of Heat and Mass Transfer*, 2006, **49**, 3075-3083.